Electronic Research Archive

https://www.aimspress.com/journal/era

ERA, 34(4): 2652–2673.
DOI: 10.3934/era.2026123
Received: 08 January 2026
Revised: 13 March 2026
Accepted: 24 March 2026
Published: 27 March 2026

Research article

Dynamical mechanisms and transitions of mixed-mode bursting in a closed-loop respiratory control model

Yilan Jiang[1] **and Lixia Duan**[2,*]

[1] School of Electrical and Control Engineering, North China University of Technology, Beijing 100144, China

[2] School of Science, North China University of Technology, Beijing 100144, China

* **Correspondence:** Email: duanlx@ncut.edu.cn.

Abstract: Abnormal respiratory rhythms, a hallmark of many respiratory diseases, largely arise from transitional firing dynamics in the pre-Bötzinger complex (pre-BötC) neurons. Mixed-mode bursting (MMB), characterized by alternating depolarization block (DB) and square-wave (SW) bursts, represents a particularly complex firing pattern of significant research interest. Based on Diekman's closed-loop respiratory control model, this study applies a fast-slow dynamical analysis and the bifurcation theory to investigate how variations in hemoglobin concentration ([Hb]) govern the emergence and disappearance of MMB. Numerical simulations show that [Hb] variations induce clear transitions between MMB and single SW bursting. A dynamical analysis reveals that the intrinsic slow variable h determines the type of individual bursting, while the slow feedback variable g_{tonic}, which is regulated by the arterial blood oxygen partial pressure, evolves on a comparable timescale and influences the global trajectories by shifting the critical bifurcation structures. The interaction between these slow variables enables the emergence of MMB. When the slow feedback pathway is fixed such that g_{tonic} remains constant, MMB can no longer be sustained. These results indicate that MMB in closed-loop systems relies on the dynamic coupling of multiple slow variables rather than on the static value of a single parameter, thus providing a dynamical mechanism for complex rhythm generation.

Keywords: pre-Bötzinger complex; closed-loop control model; mixed-mode bursting; bifurcation; depolarization block

1. Introduction

Breathing is a fundamental physiological process essential to sustain life, and abnormal respiratory rhythms are closely associated with various respiratory diseases [1–4]. Physiological studies have shown that the respiratory system can generate multiple rhythmic patterns, with dynamic transitions

between these patterns dependent on the coordinated regulation of the central nervous system network [5–8]. Among the neural structures involved in respiratory rhythm generation, the pre-Bötzinger complex (pre-BötC) is widely recognized as a key central region responsible for generating respiratory rhythms [9–12]. Experiments have confirmed that pre-BötC neurons not only generate complex rhythmic activity but also undergo a dynamic transition between different patterns, such as bursting and tonic spiking, thus providing crucial physiological insights into the diversity of respiratory rhythm patterns [5, 13–17].

To further elucidate the regulatory mechanisms that underlie respiratory rhythms, researchers have integrated physiological experiments with computational modeling to develop a variety of mathematical models that simulate the firing behaviors of pre-BötC neurons and their network dynamics. For example, the minimal neuron model proposed by Butera et al. successfully reproduced the bursting and tonic spiking activities typical of pre-BötC neurons [18, 19], and Best et al. further investigated the bursting dynamics of excitatory interneurons [20]. Notably, the persistent sodium current (I_{NaP}) was identified as a key ionic mechanism underlying stable bursting in pre-BötC neurons [12, 21–23], while the calcium-activated nonspecific cationic current (I_{CAN}) also significantly contributes to rhythm regulation [24–26]. Dunmyre et al. integrated these currents into a unified model, thus successfully simulating multiple neuronal firing patterns, including tonic spiking, square-wave bursting (SW), depolarization block (DB), and mixed-mode bursting (characterized by alternating SW and DB bursts) [27]. Subsequently, Ben-Tal and Smith pioneered the integration of a simplified lung model with a neural control model to establish a closed-loop framework for respiratory regulation [28]. Building on this foundation, Diekman et al. further integrated chemosensory, biomechanical, and metabolic processes to construct a more comprehensive closed-loop respiratory control model [29]. Based on this model, Duan et al. introduced I_{CAN} to investigate the system's dynamic response and recovery capabilities under transient hypoxia [30].

Among the various bursting patterns observed in pre-BötC neurons, mixed-mode bursting (MMB) has attracted considerable attention due to its complex structure, which features the alternation or random occurrence of multiple burst types within a single oscillatory cycle. Dunmyre et al. observed the MMB in *in vitro* experiments and proposed that its emergence relies on the synergistic interaction between I_{NaP} and I_{CAN} [27]. The two-compartment model (TB model) developed by Toporikova and Butera successfully reproduced MMB by incorporating I_{CAN} [31]. A fast-slow analysis has been widely applied in the study of nonlinear dynamical systems [32–36]. From a dynamical systems viewpoint, Wang et al. demonstrated that a two-timescale mechanism is sufficient to generate MMB [32]. Guo et al. extended the Butera model by introducing external stimuli and revealed the modulatory effects of electromagnetic radiation and externally applied currents on MMB patterns [33]. Yang et al. used a coupled pre-BötC neuron model to simulate the rhythmic transition from DB to SW bursting and finally to period-1 bursting [34]. Duan et al. further illustrated how changes in calcium concentration alter the relative position of the bifurcation curve, thereby modulating MMB dynamics [35]. Liu et al. showed that, in the pre-Bötzinger complex network, the electrical coupling facilitates in-phase spike synchronization within mixed bursters [37].

Meanwhile, the role of external stimulation in inducing MMB has also attracted attention. The Hua team demonstrated that mixed-mode bursting can be induced by both excitatory and inhibitory stimuli, thus providing important insights into its underlying dynamical mechanisms and potential association with neurological disorders such as migraines [38]. In addition, Liu et al. further confirmed

in a closed-loop respiratory control model that light stimulation can trigger a transition in neuronal firing patterns from tonic spiking to MMB [39]. Beyond external stimuli, physiological parameters within the respiratory control system and their associated feedback regulation also play crucial roles in the formation and modulation of respiratory rhythms. In a closed-loop respiratory control system, the arterial oxygen partial pressure serves as a key state variable. Through chemoreceptor feedback pathways, the oxygen partial pressure influences the central pattern generator, thereby enabling respiratory rhythms to dynamically track the body's oxygenation status.

The hemoglobin concentration ([Hb]) is a fundamental physiological determinant of the blood's oxygen-carrying capacity. Variations in the [Hb] directly affect the oxygen transport efficiency and consequently influence the maintenance and regulation of the arterial oxygen partial pressure [40]. Abnormal fluctuations in the [Hb] are associated with a variety of pathological conditions. For example, a decreased [Hb] leads to anemia, which reduces the oxygen-carrying capacity and may trigger compensatory respiratory responses [41]. However, in patients with respiratory failure, this compensatory mechanism is often limited, and anemia may paradoxically increase the risk of adverse outcomes [42]. Conversely, an elevated [Hb] is commonly observed in physiological or pathological conditions such as polycythemia and high-altitude adaptation, both of which alter the oxygen transport and respiratory regulation processes [43, 44].

Previous studies have explored the role of oxygen-related parameters in respiratory regulation. In particular, Diekman et al. demonstrated within a closed-loop respiratory control model that modulating the oxygen sensitivity gain parameters can significantly alter the respiratory rhythms, thus suggesting that changes in the oxygen transport capacity may contribute to the phenomenon of "silent hypoxemia" [45].

However, although variations in oxygen transport capacity have been shown to affect the dynamics of closed-loop respiratory control systems, the dynamical mechanisms by which the [Hb] modulates the respiratory rhythms through slow feedback structures in oxygen-feedback pathways remain insufficiently understood, particularly regarding its role in the generation and transition of MMB. Therefore, in this study, we take the [Hb] as a key control parameter that governs the strength of slow feedback in the respiratory control loop. Using fast-slow decomposition and a bifurcation analysis, we systematically examine how variations in the [Hb] affect the emergence and transition of MMB.

The remainder of the paper is organized as follows: Section 2 describes the closed-loop model and analytical methods; and Sections 3 and 4 present the main results and conclusions, respectively.

2. Model and methods

2.1. Model

Diekman et al. developed a closed-loop respiratory control model in which bursting pacemaker neurons within the pre-BötC act as the central pattern generator (CPG) for respiration. The model incorporates motor neurons (α), lung volume (vol_L), alveolar oxygen partial pressure (P_AO_2), arterial oxygen partial pressure (P_aO_2), and chemoreceptor feedback, thus encompassing the essential neural, mechanical, and chemical processes of respiration. The system dynamics are described by the following set of equations [29]:

$$\frac{dV}{dt} = \frac{1}{C}\Big(- g_K n^4 (V - E_K) - g_L (V - E_L) - g_{tonic} (V - E_{tonic})$$

$$- g_{NaP} p_\infty(V) h(V - E_{Na}) - g_{Na} m_\infty^3(V)(1 - n)(V - E_{Na})\Big), \tag{2.1}$$

$$\frac{dn}{dt} = \frac{n_\infty(V) - n}{\tau_n(V)}, \tag{2.2}$$

$$\frac{dh}{dt} = \frac{h_\infty(V) - h}{\tau_h(V)}, \tag{2.3}$$

$$\frac{d\alpha}{dt} = r_a[T](1 - \alpha) - r_d\alpha, \tag{2.4}$$

$$\frac{d\, vol_L}{dt} = E_1\alpha - E_2(\mathrm{vol}_L - \mathrm{vol}_0), \tag{2.5}$$

$$\frac{d(P_AO_2)}{dt} = \frac{P_{\mathrm{ext}}O_2 - P_AO_2}{\mathrm{vol}_L}\left[\frac{d\,\mathrm{vol}_L}{dt}\right]_+ - \frac{P_AO_2 - P_aO_2}{\tau_{LB}}, \tag{2.6}$$

$$\frac{d(P_aO_2)}{dt} = \frac{J_{LB} - J_{BT}}{\zeta\left(\beta_{O_2} + \eta\,\frac{\partial S_aO_2}{\partial P_aO_2}\right)}, \tag{2.7}$$

where V denotes the membrane potential, C denotes the membrane capacitance, and n and h represent the gating variables for the potassium (K^+) delayed rectifier and sodium (N_a^+) currents, respectively. The five terms on the right-hand side of Eq (2.1) correspond, in order, to the potassium delayed rectifier current, leak current, tonic excitatory current, persistent sodium current, and fast sodium current. The parameters g_K, g_L, g_{tonic}, g_{NaP}, and g_{Na} denote the maximal conductances of the corresponding ionic currents, while E_K, E_L, E_{tonic}, and E_{Na} represent their respective reversal potentials. α, vol_L, P_AO_2, and P_aO_2 represent the motor neuron activity, lung volume, alveolar oxygen partial pressure, and arterial oxygen partial pressure, respectively. Here, $[x]_+ = \max(x, 0)$. Equations (2.4)–(2.7) describe the dynamics of the motor pool, lung volume changes driven by motor output, regulation of alveolar oxygen partial pressure, and variations in arterial oxygen partial pressure, respectively. Additionally, chemoreceptors monitor the changes in arterial oxygen partial pressure and regulate the g_{tonic}, thereby modulating the tonic excitatory current. The expression for g_{tonic} is given as follows:

$$g_{tonic} = \phi\left[1 - \tanh\left(\frac{P_aO_2 - \theta_g}{\sigma_g}\right)\right]. \tag{2.8}$$

This regulatory mechanism enables the respiratory control system to adapt in response to the blood oxygen levels, thereby forming a closed-loop feedback control system. The voltage-dependent activation (or inactivation) function $x_\infty(V)$ and the corresponding time constant function $\tau_x(V)$ are defined as follows:

$$x_\infty(V) = \frac{1}{1 + \exp\left(\frac{V - \theta_x}{\sigma_x}\right)}, \qquad x \in \{n, h, m, p\}.$$

$$\tau_x(V) = \frac{\bar{\tau}_x}{\cosh\left(\frac{V - \theta_x}{2\sigma_x}\right)}, \qquad x \in \{n, h\}.$$

Other relevant functions are expressed as follows:

$$[T] = \frac{T_{\max}}{1 + \exp\left(-\frac{V - V_T}{K_P}\right)},$$

$$J_{LB} = \frac{P_A O_2 - P_a O_2}{\tau_{LB}} \left(\frac{\text{vol}_L}{RT} \right),$$

$$J_{BT} = M\zeta(\beta_{O_2} P_a O_2 + \eta S_a O_2),$$

$$S_a O_2 = \frac{(P_a O_2)^c}{(P_a O_2)^c + K^c},$$

$$\frac{\partial S_a O_2}{\partial P_a O_2} = c(P_a O_2)^{c-1} \left[\frac{1}{(P_a O_2)^c + K^c} - \frac{(P_a O_2)^c}{\left((P_a O_2)^c + K^c\right)^2} \right],$$

$$\zeta = \text{vol}_B \times \left(\frac{\text{mol O}_2}{22400\,\text{ml O}_2} \right),$$

$$\eta = [\text{Hb}] \times \left(\frac{1.36\,\text{ml O}_2}{g\ \text{Hb}} \right).$$

The above formulations describe the hemoglobin saturation curve and the oxygen-carrying capacity of blood. For other parameters, we refer to the definitions given in [29]. The parameter values used in the model are listed in Table 1.

Table 1. Parameter values used in the model.

Parameter	Value	Parameter	Value	Parameter	Value
C	21 pF	E_K	−85 mV	E_L	−65 mV
E_{Na}	50 mV	E_{tonic}	0 mV	g_K	7 nS
g_L	2.3 nS	g_{NaP}	2.8 nS	g_{Na}	18 nS
θ_m	−34 mV	σ_m	−5 mV	θ_n	−29 mV
σ_n	−4 mV	$\bar{\tau}_n$	10 ms	θ_h	−48 mV
σ_h	6 mV	$\bar{\tau}_h$	10000 ms	θ_p	−40 mV
σ_p	−6 mV	r_a	0.001 $\text{mM}^{-1}\text{ms}^{-1}$	r_d	0.001 $\text{mM}^{-1}\text{ms}^{-1}$
$T_{\max}$	1 mM	V_T	2 mV	K_P	5 mV
E_1	0.0025 ms^{-1}	E_2	0.4 ms^{-1}	vol_0	2 l
$P_{\text{ext}}O_2$	149.7 mmHg	τ_{LB}	500 ms	R	62.364 l mmHg K^{-1} mol^{-1}
T	310 K	M	8×10^{-6} ms^{-1}	β_{O_2}	0.03 mlO_2 lblood^{-1} mmHg^{-1}
K	26 mmHg	vol_B	5 l	c	2.5
ϕ	0.3 nS	θ_g	85 mmHg	σ_g	30 mmHg

2.2. Fast-slow analysis

Building upon Diekman's seven-dimensional closed-loop respiratory control model, this study employs the maximum relative velocity (v_x) — defined as the ratio of the maximum rate of change of a variable to its dynamic range — to characterize the time-scale properties of the system variables [29]. For [Hb] = 140 g/l, the maximum relative velocity of each variable was calculated, with results

summarized in Table 2. Under other [Hb] values (150, 200, and 250 g/l), the variations in the maximum relative velocity were found to be negligible.

Table 2. Maximum relative velocity of each variable in the model at [Hb] = 140 g/l.

x	V	n	α	h	vol_L	P_AO_2	P_aO_2
v_x	1.1423	1.304	0.032	0.0081	0.0016	0.0015	0.0013

In the Diekman model, the variables V and n evolve on an ultrafast timescale, while α and h exhibit dynamics approximately one order of magnitude slower. The variables vol_L, P_AO_2, and P_aO_2 evolve even more slowly, resulting in an overall three-timescale structure composed of ultrafast, fast, and slow components. Under the parameter settings adopted in this study, the timescale of the slow inactivation variable h becomes comparable to that of vol_L, P_AO_2, and P_aO_2. Although the maximum relative velocity of α is smaller than that of the membrane potential variables (V and n), it remains substantially larger than those of the slow feedback variables (h, vol_L, P_AO_2, and P_aO_2). Therefore, from the perspective of the timescale separation, α evolves on a timescale comparable to the fast neuronal dynamics rather than the slow physiological feedback processes. As a result, the original multi-timescale structure effectively reduces to a two-timescale system composed of a fast subsystem and a slow subsystem. Accordingly, Eqs (2.3) and (2.5)–(2.7) are grouped as the slow subsystem, while Eqs (2.1), (2.2) and (2.4) constitute the fast subsystem.

As shown in Eq (2.8), the excitatory conductance g_{tonic} monotonically varies with the arterial oxygen partial pressure P_aO_2; thus,it functions as a slow feedback modulator within the closed-loop architecture. In the subsequent analysis, g_{tonic} is adopted as an explicit representative of the P_aO_2 - mediated feedback pathway, since it is uniquely determined by P_aO_2 and evolves on the same slow timescale. Thus, together with the intrinsic slow variable h, g_{tonic} is treated as a bifurcation parameter to investigate the fast-slow dynamical mechanisms that underlie rhythm transitions in the closed-loop system.

All numerical simulations were performed in MATLAB using the stiff solver ode15s. Time integration was carried out with both the relative and absolute tolerances set to 10^{-9}. The initial conditions were specified as $V = -58$, $n = 0.00095344$, $h = 0.7454$, $\alpha = 0.00020026$, $vol_L = 2.0525$, $P_AO_2 = 98.9638$, and $P_aO_2 = 92.4247$. The total integration time was 200 s. Bifurcation analyses were performed using XPPAUT, where the continuation step size was set to 0.1 [46].

3. Results

3.1. Parameter-dependent rhythm transitions in the closed-loop system

3.1.1. Appearance and disappearance of MMB under variation of [Hb]

This section examines the dynamical behavior of the closed-loop system under variations in the [Hb], with particular emphasis on the structure of MMB and its transition to single bursting regimes. Figure 1 illustrates the membrane potential dynamics for [Hb] = 140, 150, 200, and 250 g/l. At [Hb] = 140 and 150 g/l (Figures 1(a),(b), respectively), the system exhibits a typical MMB pattern characterized by the alternating occurrence of DB and SW bursting. When the [Hb] is increased to 200 g/l (Figure 1(c)), the number of SW bursts increases, and the activity evolves into a periodic

sequence consisting of four bursts (DB:SW=1:3). A further increase in the [Hb] to 250 g/l (Figure 1(d)) leads to a complete transition to a pure SW bursting state.

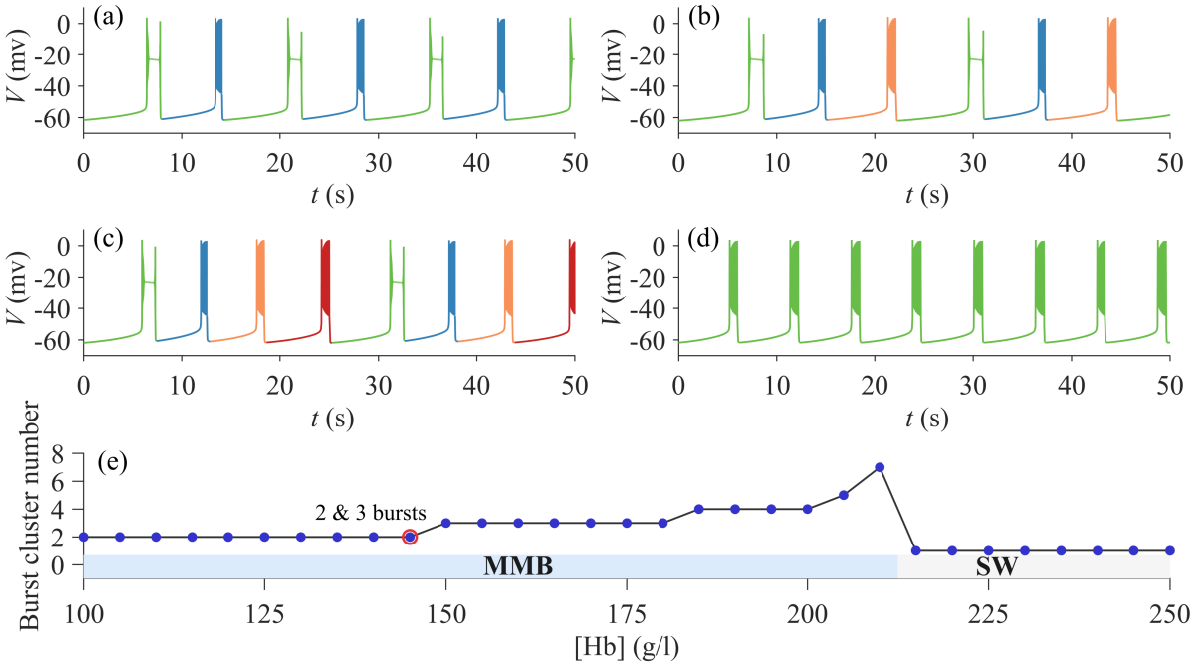

Figure 1. Membrane potential V and burst statistics for different [Hb]. (a) At [Hb] = 140 g/l, DB (green):SW (blue)= 1:1; (b) At [Hb] = 150 g/l, DB:SW = 1:2; (c) At [Hb] = 200 g/l, DB:SW = 1:3; (d) At [Hb] = 250 g/l, single bursting dominated by SW; (e) Dependence of the number of burst clusters per oscillation cycle on the [Hb].

The relationship between burst count and the [Hb] is summarized in Figure 1(e). The solid curve denotes the number of distinct bursts identified in each full oscillation cycle. The shaded background distinguishes two firing regimes: a multi-burst regime corresponding to MMB (blue region), and a single-burst regime corresponding to pure SW bursting (gray region). Circular markers indicate transition intervals where qualitative changes in the bursting mechanism occur, such as the critical region between the two- and three-burst states. At low [Hb] levels (100–140 g/l), the system predominantly maintains a two-burst mixed-mode pattern. Within an intermediate range (145–210 g/l), the burst number nonlinearly increases, ranging from two to seven, after which the multimodal characteristics of MMB gradually weaken. When the [Hb] exceeds a critical threshold of approximately 210 g/l, MMB entirely disappears and the system only exhibits regular SW bursting.

3.1.2. Fast-slow interaction and geometric mechanisms of MMB

Figure 2(a) presents the one-parameter bifurcation diagram of the fast subsystem (Eqs (2.1), (2.2) and (2.4)) with respect to the slow variable h. The gray and black curves denote the bifurcation branches corresponding to the minimum and maximum values of g_{tonic}, respectively, where solid lines indicate a stable state and dashed lines denote an unstable one state. The equilibrium branch exhibits an S-shaped structure, comprised of an upper segment (focus), a middle segment (saddle),

and a lower segment (node). As the bifurcation parameter h decreases, two saddle-node bifurcations (SN1 and SN2) occur at the turning points. The stable focus on the upper branch loses stability via a subcritical Andronov-Hopf bifurcation (H), giving rise to an unstable limit cycle. This cycle later stabilizes through a limit point of cycles (LPC) bifurcation and eventually vanishes in a saddle-homoclinic (SH) bifurcation upon collision with the saddle point on the middle branch. An increase in g_{tonic} shifts the bifurcation structure leftward, with the lower branch (SN1) undergoing a significantly larger displacement than the upper branch.

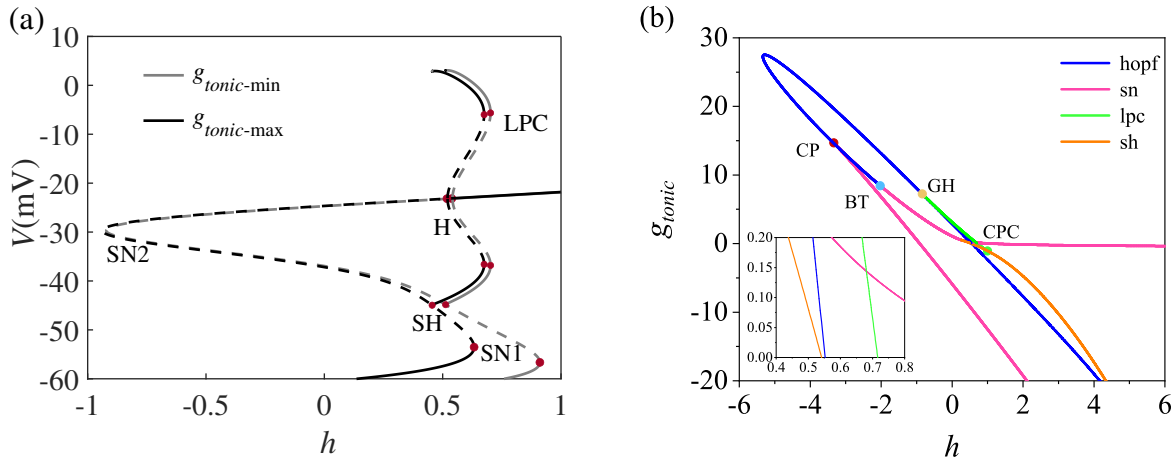

Figure 2. One- and two-parameter bifurcation diagrams of the fast subsystem. (a) One-parameter bifurcation diagram corresponding to the maximum (black) and minimum (gray) values of g_{tonic}. Solid curves denote stable equilibria or limit cycles; dashed curves indicate unstable states. (b) Two-parameter bifurcation diagram that shows Hopf (hopf, blue), saddle-node (sn, magenta), limit point of cycles (lpc, green), and saddle-homoclinic (sh, orange) bifurcation curves. Codimension-2 bifurcation points include generalized Hopf (GH), Cusp (CP), Bogdanov-Takens (BT), and Cusp of periodic cycle (CPC). The inset provides an enlarged view of the critical region associated with bursting pattern transitions.

To elucidate the regulatory mechanism that underlies MMB generation through the dynamic interplay between the slow variable h and g_{tonic}, we constructed a two-parameter bifurcation diagram in the (h, g_{tonic}) plane (Figure 2(b)). In this diagram, the hopf, sn, lpc, and sh bifurcation curves are shown in blue, magenta, green, and orange, respectively. The saddle-node (sn) and Hopf (hopf) curves intersect at a Bogdanov-Takens (BT) point, two sn curves meet at a cusp (CP) bifurcation, and the convergence of two lpc curves gives rise to a cusp bifurcation of a periodic cycle (CPC). Additionally, the transition between supercritical and subcritical Andronov-Hopf bifurcations occurs at a generalized Hopf (GH) point. The presence of these codimension-2 bifurcations highlights the system's intricate dynamical structure and its capacity to exhibit a wide range of behavioral regimes.

The multiple timescale dynamical analysis of the closed-loop respiratory control system under different [Hb] is illustrated in Figures 3(a1)–(d1), which presents the one-parameter bifurcation diagrams of the fast subsystem with respect to the slow variable h, which is superimposed with phase trajectories of the full system.

At [Hb] = 140 g/l (Figure 3(a1)), the trajectory of burst 1 (green) originates from the lower resting

state, drifts rightward along the stable node, and undergoes a rapid transition to the upper branch via the SN1 bifurcation. As it remains distant from the LPC bifurcation point, only a stable focus exists in this region; therefore, the trajectory exhibits damped oscillations around this stable focus. After crossing the Hopf (H) bifurcation, it is repelled by the unstable focus and eventually returns to the lower branch, thus ending the activity of burst 1 and restoring the resting state. This behavior identifies burst 1 as a "subHopf/subHopf" bursting pattern [47]. From a physiological perspective, this regime corresponds to a depolarization-block like state, where the membrane potential remains relatively elevated and neuronal excitability is reduced, thus resulting in a weakened or suppressed spike activity.

In contrast, burst 2 (blue) also transitions to the upper branch via SN1 but then enters the bistable region (stable focus and stable limit cycle coexist), which is located left of the LPC bifurcation. Here, the trajectory is attracted to the stable limit cycle,thus resulting in sustained oscillations that generate a SW burst. As the bifurcation parameter h further decreases, the neuronal activity ultimately terminates via an SH bifurcation, thus returning the system to rest and completing the cycle. The bursting pattern is classified as a "fold/homoclinic" type. This regime corresponds to the classical SW bursting pattern commonly observed in neuronal systems, which is characterized by sustained spiking and a relatively high neuronal excitability during the bursting phase.

At [Hb] = 150 g/l, the MMB pattern consists of one DB burster and two SW bursters (Figure 1(b)). The dynamical types of burst 1 (green) and burst 2 (blue) remain consistent with those observed at [Hb] = 140 g/l. The newly emerged burst 3 (yellow-orange) also exhibits a "fold/homoclinic" bursting pattern (Figure 3(b1)). Specifically, its trajectory transitions to the active state via the SN1 bifurcation. Although it lies to the right of the LPC bifurcation point, it is situated closer to the LPC than burst 1, thus influencing its oscillatory behavior.

When [Hb] increases to 200 g/l (Figure 3(c1)), bursts 1 and 2 retain their original dynamical properties. In contrast, burst 3 (yellow-orange) now reaches the upper branch at a position very close to the LPC bifurcation point, where the stable limit cycle becomes the dominant attractor. Once captured by this attractor, the trajectory exhibits a sustained bursting activity, which ultimately terminates via a saddle-homoclinic (SH) bifurcation. Then the system returns to the resting state, followed by the emergence of burst 4 (red), which also exhibits a "fold/homoclinic" bursting pattern. The behavior of burst 4 resembles that of burst 3 observed at [Hb] = 150 g/l.

When [Hb] increases to 250 g/l (Figure 3(d1)), the system simplifies to a single SW bursting pattern (see Figure 1(d)). The phase-plane trajectory of this burst is consistent with the SW pattern described earlier. A dynamical analysis confirms that this bursting type persists due to the underlying invariant bifurcation structure: the trajectory consistently enters the active state through an SN1 bifurcation and terminates via an SH bifurcation, following the same "fold/homoclinic" bursting mechanism.

Notably, the ranges of the bifurcation parameter h that support DB and SW bursting substantially differ, as evidenced by the contrast in oscillation amplitudes between bursts 1 and 2 in Figure 3. This disparity is further amplified by the systematic leftward shift of bifurcation curves under the regulation of g_{tonic}, which promotes the coexistence of multiple steady states in the phase plane during system evolution. Consequently, the closed-loop system can generate a wide variety of bursting patterns, thus enhancing its dynamic repertoire.

Figures 3(a2)–(d2) show the dynamical evolution trajectory of MMB within the two-parameter plane. The bifurcation structure remains consistent with that shown in Figure 2(b). The yellow shaded region denotes the parameter domain where stable limit cycles exist. As g_{tonic} increases, all

bifurcation curves shift leftward in the (h, g_{tonic}) plane, with the sn1 curve exhibiting a significantly greater displacement compared to the other bifurcation curves. The sn1 curve intersects with the lpc curve at (h, g_{tonic}) = (0.68,0.14), thus highlighting a key organizing center in the parameter space.

Bursts 1 (green), 2 (blue), 3 (brown), and 4 (red) all evolve in a counterclockwise direction, with gray arrows indicating the progression of the system during the resting phases. The key dynamical distinction between DB and SW bursting lies in the relative position of the trajectory with respect to the stable limit cycle region (yellow-shaded area) when crossing the saddle-node bifurcation curve (sn1):

1) DB bursting (Burst 1): Under all [Hb] conditions, the trajectory starts from the resting state and, as h and g_{tonic} increase, crosses sn1 while remaining outside the stable limit cycle region. In this case, only a stable focus attractor exists in the phase plane, thus resulting in transient stability. As h and g_{tonic} subsequently decrease, the trajectory sequentially crosses the hopf and sh bifurcation curves, thereby terminating Burst 1;

2) SW (Bursts 2–4): In contrast, after crossing the sn1 curve, the trajectory either remains within or enters the basin of attraction of the stable limit cycle. For instance, at [Hb] = 140 g/l (Burst 2, Figure 3(a2), the elevated g_{tonic} following Burst 1 causes the trajectory to cross sn1 above its intersection with the lpc curve, thus placing it within the stable limit cycle region. The system is subsequently attracted to the limit cycle, thus producing a burst with a gradually increasing amplitude that terminates via a sh bifurcation. At [Hb] = 150 g/l (Burst 3, Figure 3(b2), after Burst 2 ends at the sh bifurcation, the trajectory first crosses the lpc curve before approaching the sn1 curve; its proximity to the lpc allows it to be recaptured by the stable limit cycle, thereby re-entering the yellow region and generating sustained oscillations until it terminates at the sh bifurcation. At [Hb] = 200 g/l (Figure 3(c2)), two-parameter analysis confirms that Bursts 1 and 2 maintain their previous dynamics, while Burst 3 crosses sn1 inside the stable limit cycle region and exhibits SW behavior similar to Burst 2. Burst 4 follows a pattern analogous to Burst 3 at [Hb] = 150 g/l. At [Hb] = 250 g/l (Figure 3(d2)), the trajectory remains confined between the sn1 and sh curves. After each crossing of sn1, it is repeatedly drawn back into the stable limit cycle region, thus resulting in sustained SW bursting.

A bifurcation analysis reveals that the system exhibits multistability as the [Hb] varies, thus highlighting the synergistic regulation between the slow variable h and the excitatory conductance g_{tonic} in generating MMB. As the [Hb] changes, the system trajectory repeatedly traverses critical bifurcation curves (e.g., sn1 and sh) in the phase plane, thus resulting in distinct bursting patterns across different parameter regions. In particular, the alternation between DB and SW bursts gives rise to MMB. These findings demonstrate that, within a closed-loop fast-slow dynamical system, MMB patterns can emerge from the interaction between multiple timescales and the underlying bifurcation structure.

Figures 4(a)–(d) illustrate the dynamical evolution of system trajectories in the three-dimensional (h, g_{tonic}, V) space. In the parameter-space panels, the black curve in the left subpanel represents the bifurcation structure when g_{tonic} reaches its maximum value during the bursting cycle, while the gray curve in the right subpanel corresponds to the bifurcation structure at its minimum value (refer to Figures 3(a1)–(d1)). The results indicate that the resting state evolves from the region of a minimum g_{tonic} towards the maximum (right to left), whereas the bursting activity propagates in the opposite direction, from the maximum toward the minimum g_{tonic} region.

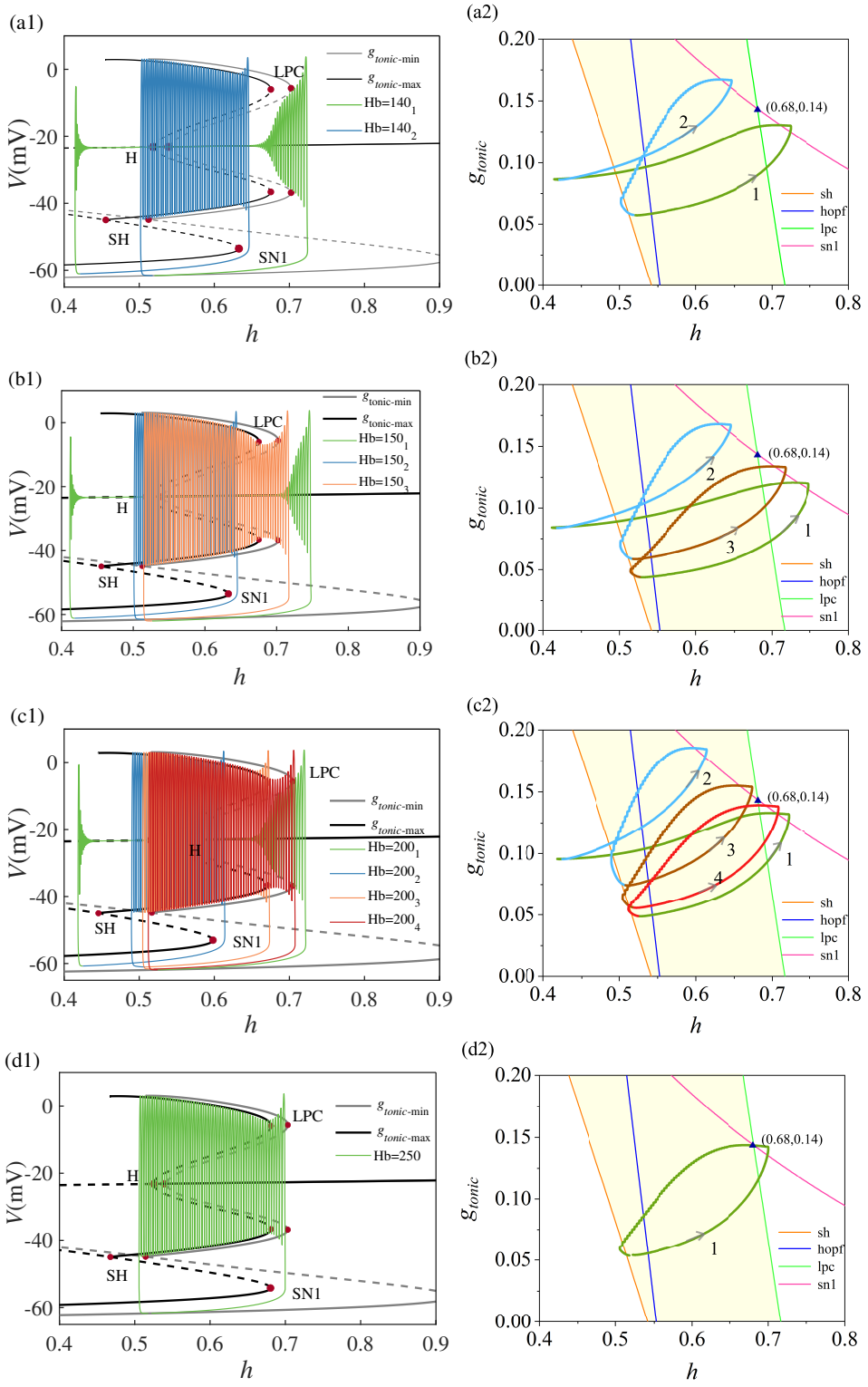

Figure 3. Multiscale dynamical analysis of the closed-loop respiratory control system under different hemoglobin concentrations ([Hb]). (a) [Hb] = 140 g/l; (b) [Hb] = 150 g/l; (c) [Hb] = 200 g/l; (d) [Hb] = 250 g/l. (a1)–(d1) Separation of fast and slow variables. (a2)–(d2) Projection of the full-system phase trajectories onto the two-parameter plane, where the numbers indicate the sequence of bursting events and gray arrows show the direction of the trajectory evolution.

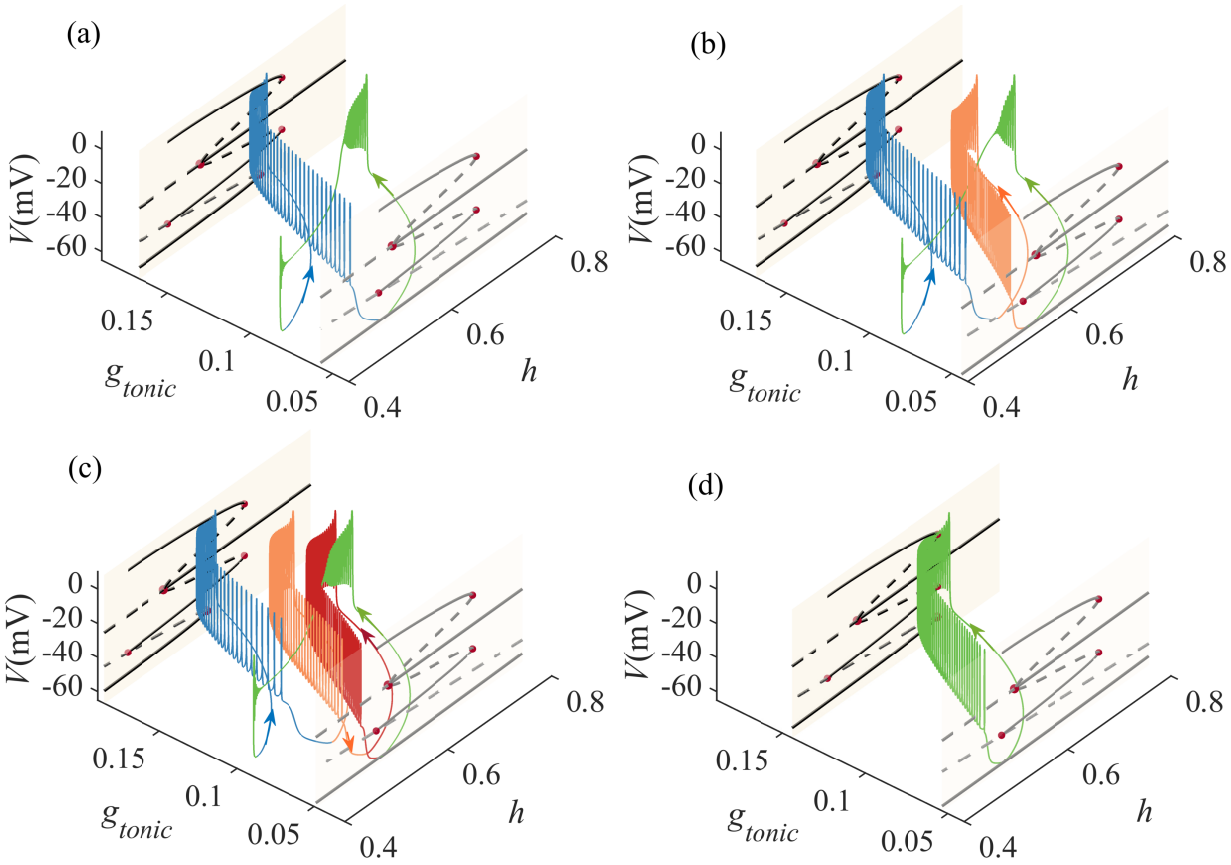

Figure 4. Bifurcation and bursting trajectories in the (h, g_{tonic}, V) space. Left panels: bifurcation at maximum g_{tonic}; Right panels: bifurcation at minimum g_{tonic}. (a) [Hb] = 140 g/l; (b) [Hb] = 150 g/l; (c) [Hb] = 200 g/l; (d) [Hb] = 250 g/l.

A comparative analysis shows that the DB pattern occupies a significantly wider range in the h-parameter space compared to SW bursting and exhibits distinct stability, as it remains unaffected by limit cycles or SH bifurcations. This stability is a fundamental characteristic of the depolarization block mechanism. In contrast, SW bursting begins when the trajectory exits the resting state via a SN1 bifurcation, undergoes a rapid transition near the extremal value of g_{tonic}, and ultimately terminates at the SH bifurcation in the minimum-gtonic region. Notably, the dynamic range of g_{tonic} variation during SW bursting is substantially larger than during DB.

Variations in the [Hb] regulate the excitatory conductance g_{tonic} via changes in the P_aO_2, thereby altering the phase space trajectory of the system. This series of cascading effects ultimately determines the emergence or disappearance of MMB. A further analysis indicates that the slow variable h plays a central role in determining the bursting type (SW or DB bursting) by governing the bifurcation structures associated with different firing patterns.

In contrast, the slow feedback variable g_{tonic}, which evolves on a comparable timescale, regulates the rhythmic activity by systematically shifting the relative positions of these bifurcation curves. However, it remains unclear whether these rhythm transitions originate from the temporal evolution of g_{tonic} or are primarily governed by its quasi-static level. To address this question, in the following section, we examine the system dynamics under a slow feedback pathway by fixing the control

variable P_aO_2, which modulates g_{tonic}, to further elucidate the role of dual slow-variable interactions in generating MMB.

3.2. Elimination of MMB under constant slow feedback

3.2.1. Freezing the slow evolution of g_{tonic} via fixed P_aO_2

As shown in Eq (2.8), g_{tonic} is defined as a monotonic and instantaneous function of P_aO_2, without additional dynamic delays or independent modulation from other state variables. Therefore, in the numerical simulations, fixing P_aO_2 at a constant value strictly fixes g_{tonic}, which is equivalent to freezing the slow feedback pathway. This procedure decouples the dynamic interaction between P_aO_2 and g_{tonic} while allowing all other variables to evolve normally, thus enabling us to distinguish the dynamical role of the slow feedback from its static parameter effect. In Section 3.1, P_aO_2 dynamically evolves with the system state, thereby driving g_{tonic} to slowly change on a comparable timescale. By shifting the relative positions of key bifurcation curves, this slow evolution enables the system trajectory to repeatedly traverse critical the bifurcation regions, thereby facilitating the emergence of MMB. To determine whether the generation of MMB depends on the dynamic evolution of the slow feedback variable g_{tonic}, rather than solely on its static level, this section considers a representative parameter setting of [Hb] = 140 g/l. Other cases ([Hb] = 150, 200, and 250 g/l) exhibit qualitatively similar dynamical behaviors and are therefore omitted for brevity. By clamping P_aO_2, g_{tonic} is held constant throughout the system evolution, allowing us to examine the firing rhythm under a frozen slow-feedback condition and to isolate the role of slow-variable dynamics in shaping MMB.

When the system initially exhibited a MMB rhythm composed of one DB burst and one SW burst, P_aO_2 was fixed at 60 mmHg at $t = 50$ s for a duration of 20 s (Figure 5(a)). During the clamp, g_{tonic} no longer varied with the system state but remained fixed. The numerical results show that the original MMB rhythm quickly disappeared, and the electrical activity of the system transitioned to a sustained high-frequency tonic spiking state. This firing pattern functionally corresponds to a high-frequency drive in the respiratory center, which is typically associated with accelerated rhythmic states such as tachypnea. After the interference was removed, the system failed to spontaneously return to the original MMB rhythm and instead remained in the tonic spiking mode.

With P_aO_2 fixed at 80 mmHg (Figure 5(b)), the oscillation period of the membrane potential shortened, the firing frequency increased, and the original MMB changed into a pure SW pattern. Following the perturbation, the system gradually recovered to its pre-intervention state within approximately 30 s. Similarly, when P_aO_2 was set to 100 mmHg (Figure 5(c)), the system also switched from MMB to a pure SW bursting mode and was able to autonomously recover; however, its dynamical characteristics differed from those at 80 mmHg: during the intervention, the burst period increased and the firing frequency decreased, while the time required for the system to return to the initial rhythm was shorter. Figure 5(d) shows the response when P_aO_2 was fixed at 110 mmHg. Although the system retained a basic ability to recover, the neuronal electrical activity was markedly suppressed during the clamp, and the system briefly entered a firing-suppressed state. After the interference was removed, the system rapidly reverted to its original rhythm, thus indicating that this state corresponds to a transient dynamical suppression rather than a structural disruption of the rhythm.

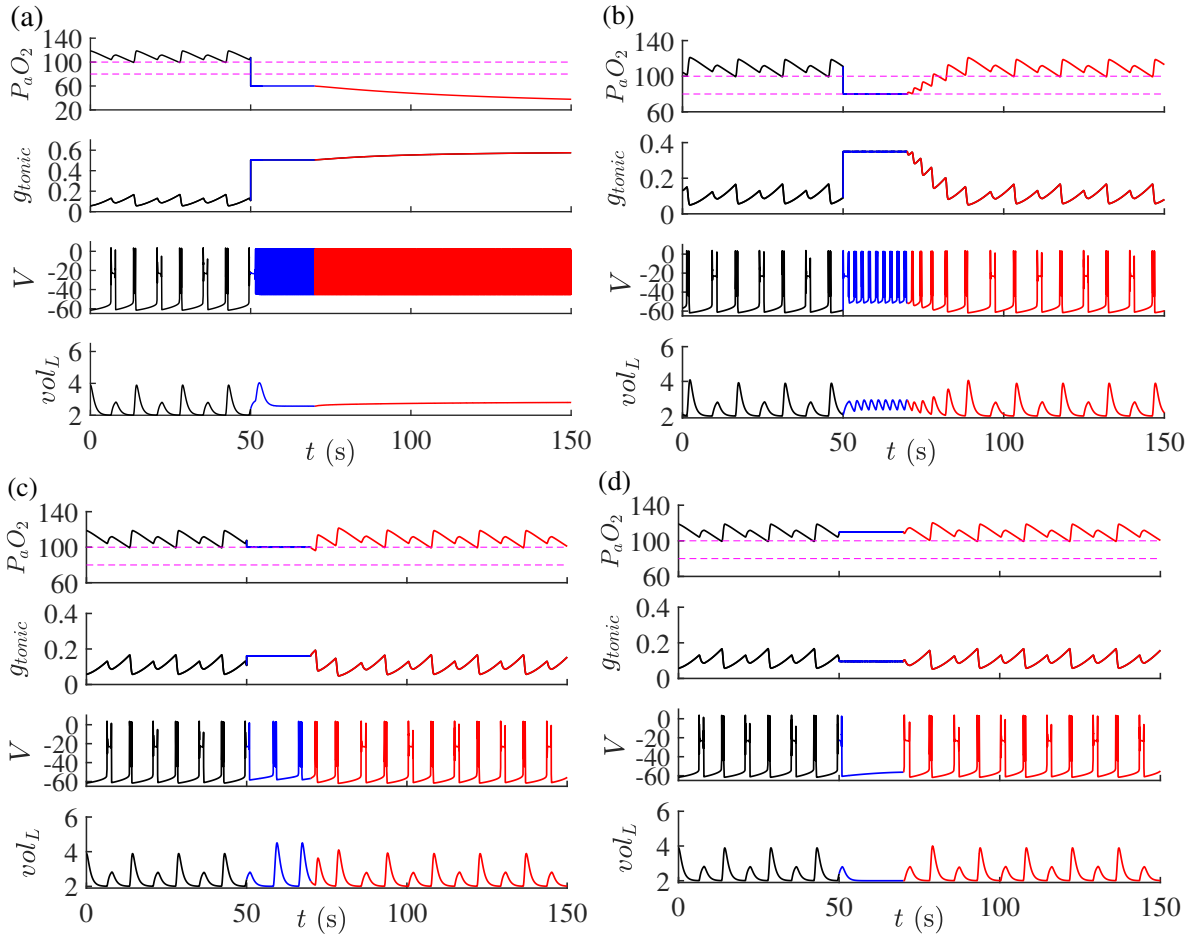

Figure 5. Responses of the closed-loop system under fixed P_aO_2 at [Hb] = 140 g/l. Black curves denote the pre-intervention state, blue curves indicate the interval during which P_aO_2 is fixed, and red curves show the post-intervention response. (a) P_aO_2 = 60 mmHg: fixing P_aO_2 induces a transition from MMB to tonic spiking; (b) P_aO_2 = 80 mmHg: fixing P_aO_2 suppresses MMB and yields a single SW with shortened periods; (c) P_aO_2 = 100 mmHg: the system exhibits a single SW during the fixed-parameter interval, with longer periods and a reduced firing frequency; (d) P_aO_2 = 110 mmHg: fixing P_aO_2 at a high level leads to strong suppression of the neuronal activity, with markedly attenuated membrane potential oscillations.

In summary, under all P_aO_2 clamp conditions, the system no longer exhibited MMB but instead transitioned to spiking, pure SW bursting, or electrically suppressed states. This demonstrates that when the dynamic evolution of the slow feedback variable g_{tonic} is inhibited, the system cannot sustain the rhythmic structure necessary for MMB.

3.2.2. Bifurcation structure associated with the disappearance of MMB

The two-parameter bifurcation curves are presented in Figure 6. As P_aO_2 decreases, the sn1 (magenta) bifurcation curve markedly shifts leftward in the (h, g_{tonic}) plane. When P_aO_2 decreases from 110 mmHg to 60 mmHg, the corresponding bifurcation parameter h for sn1 decreases from 0.809 to 0.272, thus yielding a displacement of 0.537. In contrast, the h values associated with the sh (orange),

lpc (green), and hopf (blue) bifurcations only vary by 0.224, 0.099, and 0.078, respectively. These results demonstrate that the displacement of sn1 is substantially larger than that of the other bifurcation curves. This asymmetric shift fundamentally alters the relative topological arrangement between sn1 and key bifurcation curves such as lpc and sh.

When P_aO_2 is fixed, g_{tonic} no longer dynamically evolves with the system state. As a consequence, the system trajectories are unable to repeatedly traverse the bifurcation curves in the parameter plane, thereby disrupting the dual slow-variable feedback mechanism required to sustain MMB. As sn1 shifts leftward and progressively approaches sh, the trajectory, after crossing sn1, encounters sh more rapidly, thus leading to the earlier termination of each burst and a shortening of the bursting period. With a further reduction of P_aO_2, this compression of the bifurcation structure ultimately drives the system into a regime of sustained tonic spiking.

Figure 7 illustrates the one-parameter bifurcation structures of the fast subsystem for different fixed P_aO_2 levels (60, 80, 100 and 110 mmHg) under the condition [Hb] = 140 g/l. Although Figures 7(a)–(d) exhibit qualitatively similar overall structures, the relative positions of the key bifurcation points substantially differ. At P_aO_2 = 60 mmHg (Figure 7(a)), SN1 and SH are in proximity, thereby confining the system trajectory within the attraction domain of the stable limit cycle and thus sustaining a tonic spiking state. At P_aO_2 = 80 mmHg (Figure 7(b)), the more pronounced rightward shift of SN1 relative to SH allows the trajectory to jump to the upper branch, enter the stable limit cycle, and subsequently terminate via SH, thus forming a characteristic "fold/homoclinic" bursting pattern. In contrast, at P_aO_2 = 100 mmHg (Figure 7(c)), SN1 moves closer to LPC, thus leading to an extended burst duration and an increased number of spikes within each burst. When P_aO_2 increases to 110 mmHg (Figure 7(d)), SN1 shifts to the right of LPC, thus trapping the system trajectory near the stable node on the lower branch and markedly suppressing the neuronal firing activity.

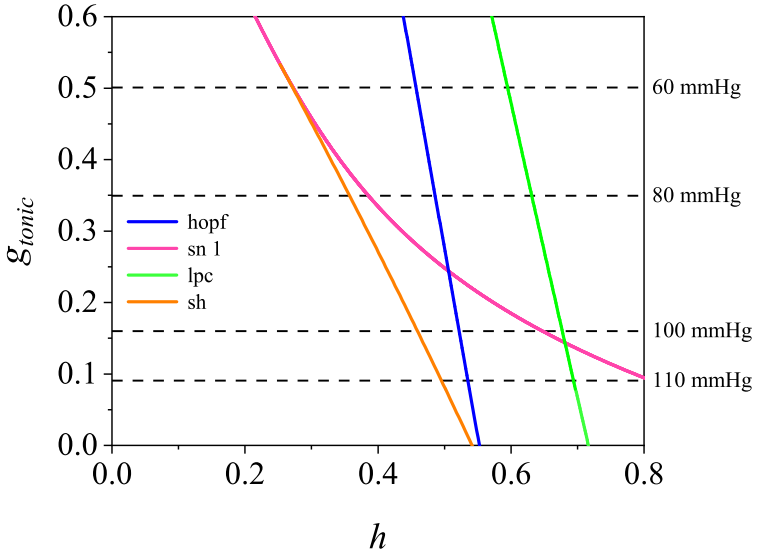

Figure 6. Bifurcations in the (h, g_{tonic}) plane of the fast subsystem. Black dashed lines indicate g_{tonic} values at P_aO_2 = 60, 80, 100, and 110 mmHg. As P_aO_2 decreases, the sn1 curve shifts leftward toward the sh curve, thereby modifying bifurcation sequences and altering bursting patterns.

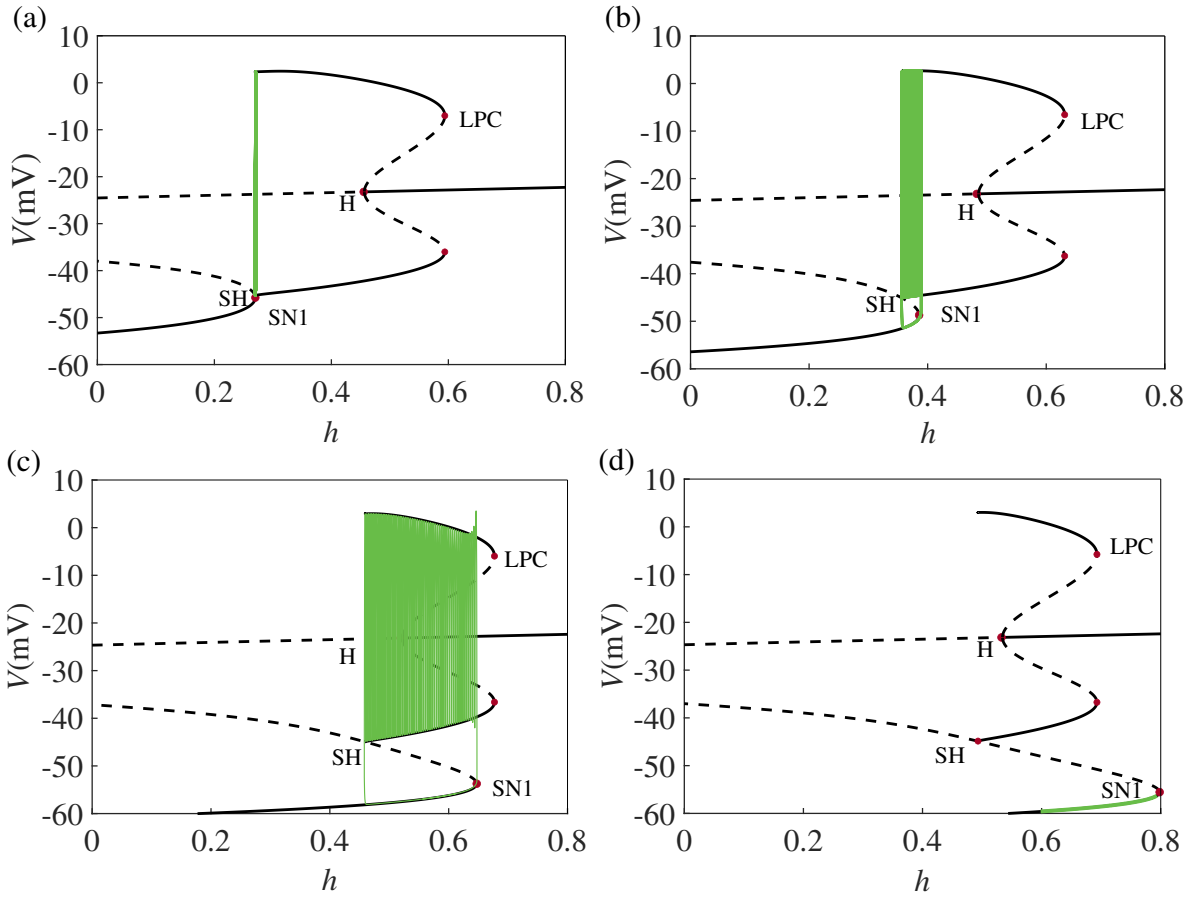

Figure 7. Fast-slow decomposition of the system at [Hb] = 140 g/l under different P_aO_2. (a) P_aO_2 = 60 mmHg; (b) P_aO_2 = 80 mmHg; (c) P_aO_2 = 100 mmHg; (d) P_aO_2 = 110 mmHg.

These results indicate that the diversity of firing rhythms observed in the system, including tonic spiking, SW bursting with different periods, and quiescent states, is primarily regulated by the slow variable h. However, when the slow feedback variable g_{tonic} is held constant, the evolution of h alone is insufficient to drive the system trajectory through the sequence of bifurcation transitions required to sustain MMB. Consequently, the emergence of MMB in the closed-loop system is not determined by a fixed value of g_{tonic}, but instead critically depends on its dynamic modulation over time.

4. Discussion

MMB is an important and complex neuronal firing pattern observed in the pre-BötC, which is the core structure responsible for respiratory rhythm generation. Within a single oscillatory cycle, different types of bursts alternate, exhibiting characteristic multiscale dynamical features. In recent years, the physiological basis of MMB has been increasingly supported by experimental evidence. For example, Dunmyre et al. confirmed the presence of MMB in pre-BötC slice preparations through in vitro electrophysiological recordings [27]. Subsequently, Chevalier et al. further demonstrated in embryonic mouse brain slices that this rhythmic pattern depends on the dynamic balance between the persistent sodium current and the calcium-activated nonspecific cationic current [48]. These findings

not only verify the biological existence of MMB but also provide an important physiological foundation for theoretical models that describe respiratory rhythm regulation.

Building on these experimental insights, Diekman and colleagues developed a closed-loop respiratory control model based on the pre-BötC rhythmogenic network and incorporated peripheral chemosensory feedback. In this framework, the P_aO_2 serves as a key feedback signal that regulates the rhythmic output of the central pattern generator through chemoreceptor pathways, thereby enabling respiratory rhythms to dynamically respond to the body's oxygenation state. As a fundamental physiological determinant of the blood's oxygen-carrying capacity, the [Hb] influences the oxygen transport efficiency and consequently affects the dynamical evolution of the P_aO_2 ((Figure 8)). Therefore, the [Hb] becomes an important physiological parameter that influences the stability and regulation of the closed-loop respiratory control system.

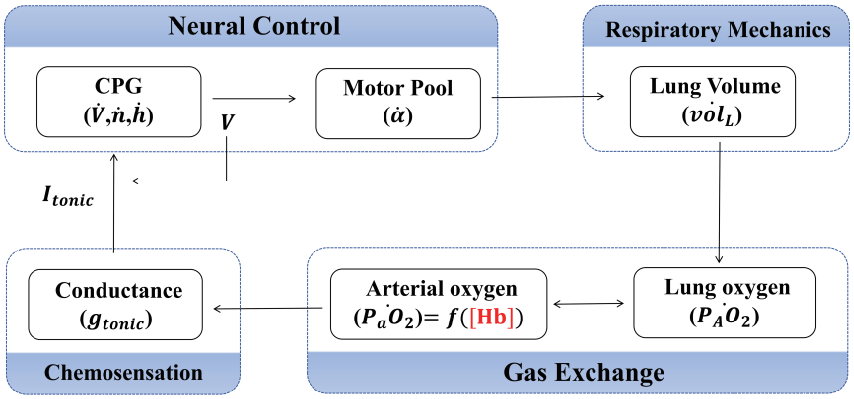

Figure 8. Schematic diagram of the closed-loop respiratory control model,adapted from [29].

Based on a closed-loop respiratory control model, this study uses the [Hb] to characterize variations in oxygen pressure-related slow feedback modulation and systematically investigates the formation of MMB and its transitions under [Hb] modulation from a dynamical systems perspective. The results show that variations in the [Hb] can induce clear transitions between MMB and single SW bursting. At relatively low [Hb] levels, the system exhibits typical MMB behavior, which is characterized by alternating DB and SW bursts within each oscillation cycle. As the [Hb] increases, the number of bursts per cycle changes nonlinearly, the multimodal structure of MMB gradually diminishes, and the system eventually stabilizes into a single-mode SW bursting pattern. This transition reflects a reorganization of the fast-slow dynamical interaction rather than a qualitative change in the intrinsic dynamics of the fast subsystem.

Fast-slow decomposition and a bifurcation analysis further reveal that the bursting type is primarily governed by the slow variable h, which determines the admissible bifurcation structures associated with different firing modes. Meanwhile, the slow feedback variable g_{tonic}, regulated by the slow evolution of P_aO_2, evolves on a comparable timescale and modulates the global organization of rhythmic activity by shifting the relative positions of critical bifurcation curves. The interaction between h and g_{tonic} enables the system trajectories to traverse multiple bifurcation regions within a single period, thereby

giving rise to MMB.

To further clarify whether MMB depends on the dynamic evolution of the slow feedback variable g_{tonic} rather than merely its steady-state level, P_aO_2 was fixed to constrain the evolution of g_{tonic}. Under all fixed-P_aO_2 conditions, the system no longer exhibits MMB; instead, it transitions to tonic spiking, single SW bursting, or a suppressed activity depending on the parameter level. Notably, although the intrinsic slow variable h continues to evolve, its isolated action is insufficient to sustain MMB. These observations indicate that MMB in the closed-loop system is not determined by a specific static value of the slow feedback variable g_{tonic}, but instead relies on its time-dependent modulation in coordination with intrinsic slow dynamics.

From a dynamical systems perspective, this study elucidates how slow feedback regulation organizes complex discharge patterns and extends the theoretical understanding of multiscale interaction mechanisms that underlie MMB. In particular, our findings are consistent with the results of Wang et al., who demonstrated that MMB dynamics can arise from interactions between two temporal scales [32].

It should be noted that the present analysis is based on a simplified closed-loop respiratory control model. The model does not yet account for the heterogeneity of pre-BötC neuronal populations, nor does it incorporate important physiological feedback mechanisms such as CO_2 chemosensitivity. Therefore, future work could examine the robustness of these results within more comprehensive modeling frameworks, for example, by introducing CO_2 chemosensory feedback [49, 50], thereby considering heterogeneous neuronal populations, or experimentally validating model predictions using in vitro pre-BötC slice preparations. Furthermore, developing a hardware emulator for the proposed model represents a promising direction for future research. As discussed in [51], such an emulator could be implemented either digitally using low-cost microcontrollers or through analog electronic circuits. In particular, an analog emulator would provide a robust platform for the real-time investigation of the nonlinear dynamics that underlie multiscale mixed-bursting patterns.

Use of AI tools declaration

The authors declare they have not used Artificial Intelligence (AI) tools in the creation of this article.

Acknowledgments

This work is supported by the National Natural Science Foundation of China (Grant No.12272002) and the North China University of Technology (Grant Nos.2023XN075-01,2023YZZKY19).

Conflict of interest

Professor Lixia Duan is an editorial board member for Electronic Research Archive and was not involved in the editorial review and the decision to publish this article. The authors declare there are no conflicts of interest.

References

1. M. Gorini, A. Spinelli, R. Ginanni, R. Duranti, F. Gigliotti, G. Scano, Neural respiratory drive and neuromuscular coupling in patients with chronic obstructive pulmonary disease (COPD), *Chest*, **98** (1990), 1179–1186. https://doi.org/10.1378/chest.98.5.1179
2. M. Gorini, G. Misuri, A. Corrado, R. Duranti, I. Iandelli, E. De Paola, et al., Breathing pattern and carbon dioxide retention in severe chronic obstructive pulmonary disease, *Thorax*, **51** (1996), 677–683. https://doi.org/10.1136/thx.51.7.677
3. R. B. Gorman, D. K. McKenzie, N. B. Pride, J. F. Tolman, S. C. Gandevia, Diaphragm length during tidal breathing in patients with chronic obstructive pulmonary disease, *Am. J. Respir. Crit. Care Med.*, **166** (2002), 1461–1469. https://doi.org/10.1164/rccm.200111-087OC
4. R. L. Horner, Pathophysiology of obstructive sleep apnea, *J. Cardiopulmonary Rehabil. Prev.*, **28** (2008), 289–298. https://doi.org/10.1097/01.HCR.0000336138.71569.a2
5. J. L. Feldman, C. A. Del Negro, Looking for inspiration: new perspectives on respiratory rhythm, *Nat. Rev. Neurosci.*, **7** (2006), 232–241. https://doi.org/10.1038/nrn1871
6. S. P. Lieske, M. Thoby-Brisson, P. Telgkamp, J. M. Ramirez, Reconfiguration of the neural network controlling multiple breathing patterns: eupnea, sighs and gasps, *Nat. Neurosci.*, **3** (2000), 600–607. https://doi.org/10.1038/75776
7. P. Banovcin, J. Seidenberg, H. von der Hardt, Assessment of tidal breathing patterns for monitoring of bronchial obstruction in infants, *Pediatr. Res.*, **38** (1995), 218–220. https://doi.org/10.1203/00006450-199508000-00014
8. A. K. Tryba, F. Peña, S. P. Lieske, J. C. Viemari, M. Thoby-Brisson, J. M. Ramirez, Differential modulation of neural network and pacemaker activity underlying eupnea and sigh-breathing activities, *J. Neurophysiol.*, **99** (2008), 2114–2125. https://doi.org/10.1152/jn.01192.2007
9. A. L. Bianchi, M. Denavit-Saubié, J. Champagnat, Central control of breathing in mammals: neuronal circuitry, membrane properties, and neurotransmitters, *Physiol. Rev.*, **75** (1995), 1–45. https://doi.org/10.1152/physrev.1995.75.1.1
10. M. I. Cohen, Neurogenesis of respiratory rhythm in the mammal, *Physiol. Rev.*, **59** (1979), 1105–1173. https://doi.org/10.1152/physrev.1979.59.4.1105
11. D. W. Richter, K. Ballanyi, S. Schwarzacher, Mechanisms of respiratory rhythm generation, *Curr. Opin. Neurobiol.*, **2** (1992), 788–793. https://doi.org/10.1016/0959-4388(92)90135-8
12. I. A. Rybak, A. P. L. Abdala, S. N. Markin, J. F. R. Paton, J. C. Smith, Spatial organization and state-dependent mechanisms for respiratory rhythm and pattern generation, *Prog. Brain Res.*, **165** (2007), 201–220. https://doi.org/10.1016/S0079-6123(06)65013-9
13. J. C. Smith, H. H. Ellenberger, K. Ballanyi, D. W. Richter, J. L. Feldman, Pre-Bötzinger complex: a brainstem region that may generate respiratory rhythm in mammals, *Science*, **254** (1991), 726–729. https://doi.org/10.1126/science.1683005
14. S. M. Johnson, J. C. Smith, G. D. Funk, J. L. Feldman, Pacemaker behavior of respiratory neurons in medullary slices from neonatal rat, *J. Neurophysiol.*, **72** (1994), 2598–2608. https://doi.org/10.1152/jn.1994.72.6.2598

15. J. C. Rekling, J. L. Feldman, PreBötzinger complex and pacemaker neurons: hypothesized site and kernel for respiratory rhythm generation, *Annu. Rev. Physiol.*, **60** (1998), 385–405. https://doi.org/10.1146/annurev.physiol.60.1.385

16. N. Koshiya, J. C. Smith, Neuronal pacemaker for breathing visualized in vitro, *Nature*, **400** (1999), 360–363. https://doi.org/10.1038/22540

17. C. A. Del Negro, S. M. Johnson, R. J. Butera, J. C. Smith, Models of respiratory rhythm generation in the pre-Bötzinger complex. III. Experimental tests of model predictions, *J. Neurophysiol.*, **86** (2001), 59–74. https://doi.org/10.1152/jn.2001.86.1.59

18. R. J. Butera, J. Rinzel, J. C. Smith, Models of respiratory rhythm generation in the pre-Bötzinger complex. I. Bursting pacemaker neurons, *J. Neurophysiol.*, **82** (1999), 382–397. https://doi.org/10.1152/jn.1999.82.1.382

19. R. J. Butera, J. Rinzel, J. C. Smith, Models of respiratory rhythm generation in the pre-Bötzinger complex. II. Populations of coupled pacemaker neurons, *J. Neurophysiol.*, **82** (1999), 398–415. https://doi.org/10.1152/jn.1999.82.1.398

20. J. Best, A. Borisyuk, J. Rubin, D. Terman, M. Wechselberger, The dynamic range of bursting in a model respiratory pacemaker network, *SIAM J. Appl. Dyn. Syst.*, **4** (2005), 1107–1139. https://doi.org/10.1137/050625540

21. R. H. Lee, C. J. Heckman, Essential role of a fast persistent inward current in action potential initiation and control of rhythmic firing, *J. Neurophysiol.*, **85** (2001), 472–475. https://doi.org/10.1152/jn.2001.85.1.472

22. J. F. R. Paton, A. P. L. Abdala, H. Koizumi, J. C. Smith, W. M. St John, Respiratory rhythm generation during gasping depends on persistent sodium current, *Nat. Neurosci.*, **9** (2006), 311–313. https://doi.org/10.1038/nn1650

23. R. W. Pace, D. D. Mackay, J. L. Feldman, C. A. Del Negro, Role of persistent sodium current in mouse preBötzinger complex neurons and respiratory rhythm generation, *J. Physiol.*, **580** (2007), 485–496. https://doi.org/10.1113/jphysiol.2006.124602

24. R. W. Pace, D. D. Mackay, J. L. Feldman, C. A. Del Negro, Inspiratory bursts in the preBötzinger complex depend on a calcium-activated nonspecific cation current linked to glutamate receptors in neonatal mice, *J. Physiol.*, **582** (2007), 113–125. https://doi.org/10.1113/jphysiol.2007.133660

25. E. A. Crowder, M. S. Saha, R. W. Pace, H. Zhang, G. D. Prestwich, C. A. Del Negro, Phosphatidylinositol 4,5-bisphosphate regulates inspiratory burst activity in the neonatal mouse preBötzinger complex, *J. Physiol.*, **582** (2007), 1047–1058. https://doi.org/10.1113/jphysiol.2007.134577

26. J. E. Rubin, J. A. Hayes, J. L. Mendenhall, C. A. Del Negro, Calcium-activated nonspecific cation current and synaptic depression promote network-dependent burst oscillations, *Proc. Natl. Acad. Sci. U.S.A.*, **106** (2009), 2939–2944. https://doi.org/10.1073/pnas.0808776106

27. J. R. Dunmyre, C. A. Del Negro, J. E. Rubin, Interactions of persistent sodium and calcium-activated nonspecific cationic currents yield dynamically distinct bursting regimes in a model of respiratory neurons, *J. Comput. Neurosci.*, **31** (2011), 305–328. https://doi.org/10.1007/s10827-010-0311-y

28. A. Ben-Tal, J. C. Smith, A model for control of breathing in mammals: coupling neural dynamics to peripheral gas exchange and transport, *J. Theor. Biol.*, **251** (2008), 480–497. https://doi.org/10.1016/j.jtbi.2007.12.018
29. C. O. Diekman, P. J. Thomas, C. G. Wilson, Eupnea, tachypnea, and autoresuscitation in a closed-loop respiratory control model, *J. Neurophysiol.*, **118** (2017), 2194–2215. https://doi.org/10.1152/jn.00170.2017
30. L. Duan, X. Chen, L. Xia, Z. Wang, Dynamics and control of mixed bursting in nonlinear pre-Bötzinger complex systems, *Nonlinear Dyn.*, **112** (2024), 8539–8556. https://doi.org/10.1007/s11071-024-09473-3
31. N. Toporikova, R. J. Butera, Two types of independent bursting mechanisms in inspiratory neurons: an integrative model, *J. Comput. Neurosci.*, **30** (2011), 515–528. https://doi.org/10.1007/s10827-010-0274-z
32. Y. Wang, J. E. Rubin, Multiple timescale mixed bursting dynamics in a respiratory neuron model, *J. Comput. Neurosci.*, **41** (2016), 245–268. https://doi.org/10.1007/s10827-016-0616-6
33. D. D. Guo, Z. S. Lü, Effect of magnetic flow and external forcing current on mixed bursting in the pre-Bötzinger complex, *Chin. Phys. B*, **28** (2019), 110501. https://doi.org/10.1088/1674-1056/ab43b9
34. Y. Yang, Y. Li, H. Gu, Synchronization transition from bursting to spiking and bifurcation mechanism of the pre-Bötzinger complex, *Acta Phys. Sin.*, **69** (2020), 040501. https://doi.org/10.7498/aps.69.20191509
35. L. Duan, T. Liang, Y. Zhao, H. Xi, Multi-time scale dynamics of mixed depolarization block bursting, *Nonlinear Dyn.*, **103** (2021), 1043–1053. https://doi.org/10.1007/s11071-020-05744-x
36. Y. Shao, F. Wu, Q. Wang, Bursting dynamics and synchronization of neuromorphic systems with VO_2 memristors and Josephson junctions, *Nonlinear Dyn.*, **113** (2025), 33907–33926. https://doi.org/10.1007/s11071-025-11757-1
37. M. Liu, L. Duan, In-phase and anti-phase spikes synchronization within mixed bursters of the pre-Bötzinger complex, *Electron. Res. Arch.*, **30** (2022), 961–977. https://doi.org/10.3934/era.2022050
38. H. Hua, H. Gu, Y. Jia, Y. Li, Opposite stimulations can induce a same mixed-mode neuronal bursting containing four phases: underlying two-parameter bifurcations and threshold, *Nonlinear Dyn.*, **113** (2025), 25153–25173. https://doi.org/10.1007/s11071-025-11387-7
39. M. Liu, L. Duan, Dynamics and bifurcation mechanisms of respiratory patterns under optogenetic intervention, *Nonlinear Dyn.*, **113** (2025), 20149–20168. https://doi.org/10.1007/s11071-025-11179-z
40. J. A. Collins, A. Rudenski, J. Gibson, L. Howard, R. O'Driscoll, Relating oxygen partial pressure, saturation and content: the haemoglobin–oxygen dissociation curve, *Breathe*, **11** (2015), 194–201. https://doi.org/10.1183/20734735.001415

41. A. Rizvi, P. Macedo, L. Babawale, H. C. Tighe, J. M. B. Hughes, J. E. Jackson, et al., Hemoglobin is a vital determinant of arterial oxygen content in hypoxemic patients with pulmonary arteriovenous malformations, *Ann. Am. Thorac. Soc.*, **14** (2017), 903–911. https://doi.org/10.1513/AnnalsATS.201611-872OC

42. D. R. Ouellette, The impact of anemia in patients with respiratory failure, *Chest*, **128** (2005), 576S–582S. https://doi.org/10.1378/chest.128.5_suppl_2.576S

43. J. S. Windsor, G. W. Rodway, Heights and haematology: the story of haemoglobin at altitude, *Postgrad. Med. J.*, **83** (2007), 148–151. https://doi.org/10.1136/pgmj.2006.049734

44. S. Tang, W. Zhou, L. Chen, H. Yan, L. Chen, F. Luo, High altitude polycythemia and its maladaptive mechanisms: an updated review, *Front. Med.*, **11** (2024), 1448654. https://doi.org/10.3389/fmed.2024.1448654

45. C. O. Diekman, P. J. Thomas, C. G. Wilson, COVID-19 and silent hypoxemia in a minimal closed-loop model of the respiratory rhythm generator, *Biol. Cybern.*, **118** (2024), 145–163. https://doi.org/10.1007/s00422-024-00989-w

46. B. Ermentrout, Simulating, analyzing, and animating dynamical systems: a guide to XPPAUT for researchers and students, *Appl. Mech. Rev.*, **56** (2003), B53. https://doi.org/10.1115/1.1579454

47. E. M. Izhikevich, Neural excitability, spiking and bursting, *Int. J. Bifurcation Chaos*, **10** (2000), 1171–1266. https://doi.org/10.1142/S0218127400000840

48. M. Chevalier, N. Toporikova, J. Simmers, M. Thoby-Brisson, Development of pacemaker properties and rhythmogenic mechanisms in the mouse embryonic respiratory network, *eLife*, **5** (2016), e16125. https://doi.org/10.7554/eLife.16125

49. Y. I. Molkov, N. A. Shevtsova, C. Park, A. Ben-Tal, J. C. Smith, J. E. Rubin, A closed-loop model of the respiratory system: focus on hypercapnia and active expiration, *PLoS One*, **9** (2014), e109894. https://doi.org/10.1371/journal.pone.0109894

50. Y. I. Molkov, J. E. Rubin, I. A. Rybak, J. C. Smith, Computational models of the neural control of breathing, *WIREs Syst. Biol. Med.*, **9** (2017), e1371. https://doi.org/10.1002/wsbm.1371

51. A. Buscarino, L. Fortuna, M. Frasca, *Essentials of Nonlinear Circuit Dynamics with MATLAB® and Laboratory Experiments*, CRC Press, 2017. https://doi.org/10.1201/b22063